

## Article

# Regularities of Changes in the Structure of Different Phases of Deformed Zirconium Alloys as a Result of Raising the Annealing Temperature According to Texture Analysis Data

Margarita Isaenkova <sup>1,\*</sup>, Olga Krymskaya <sup>1</sup>, Kristina Klyukova <sup>1</sup>, Anastasya Bogomolova <sup>1</sup>, Ilya Kozlov <sup>1,2</sup>, Pavel Dzhumaev <sup>1</sup> , Vladimir Fesenko <sup>1</sup> and Roman Svetogorov <sup>2</sup> 

<sup>1</sup> Materials Science Department, National Research Nuclear University “MEPhI”, Moscow 115409, Russia; oakrymskaya@mephi.ru (O.K.); tinakyukova@gmail.com (K.K.)

<sup>2</sup> National Research Center “Kurchatov Institute”, Moscow 123182, Russia

\* Correspondence: mgisaenkova@mephi.ru; Tel.: +7-909-683-34-78

**Abstract:** Based on the data of synchrotron and electron microscopic studies of deformed and annealed Russian zirconium alloys, the possibility of analyzing the structural-phase state and crystallographic texture of individual phases has been demonstrated. A qualitative and quantitative phase analysis of deformed and annealed tubes made of Zr-Nb-(Sn-Fe-O) alloys was carried out using diffraction patterns obtained with synchrotron radiation. The main  $\alpha$ -Zr phase and the following additional phases:  $\beta$ -Nb,  $\beta$ -Zr, and the Laves phase (intermetallic compound  $Zr(Nb,Fe)_2$ ), were found in the alloys. According to the results of texture analysis of all phases present in the alloy, the mechanisms of plastic deformation, recrystallization, and phase transformations of the main and additional phases were established. It is shown that during plastic deformation of the Zr-1%Nb alloy, a dynamic phase transformation  $\beta$ -Nb  $\rightarrow$   $\alpha$ -Zr  $\rightarrow$   $\beta$ -Zr is observed. It is established that during recrystallization, larger grains of  $\alpha$ -Zr are misoriented relative to the deformed matrix by rotating the prismatic axes around the basal axes by  $30^\circ$ , while fine grains are improved by polygonization and maintain the orientation of the deformed matrix. Processes for changing the orientation of grains of additional phases as a result of high-temperature annealing are also considered.

**Keywords:** zirconium alloys; deformation; recrystallization; crystallographic texture; electron microscopy; synchrotron radiation; X-ray radiation



**Citation:** Isaenkova, M.; Krymskaya, O.; Klyukova, K.; Bogomolova, A.; Kozlov, I.; Dzhumaev, P.; Fesenko, V.; Svetogorov, R. Regularities of Changes in the Structure of Different Phases of Deformed Zirconium Alloys as a Result of Raising the Annealing Temperature According to Texture Analysis Data. *Metals* **2023**, *13*, 1784. <https://doi.org/10.3390/met13101784>

Academic Editor: Roumen Petrov

Received: 14 September 2023

Revised: 16 October 2023

Accepted: 19 October 2023

Published: 21 October 2023



**Copyright:** © 2023 by the authors. Licensee MDPI, Basel, Switzerland. This article is an open access article distributed under the terms and conditions of the Creative Commons Attribution (CC BY) license (<https://creativecommons.org/licenses/by/4.0/>).

## 1. Introduction

Crystallographic texture is a sensitive indicator of the processes of plastic deformation, recrystallization, and phase transformations in multiphase alloys. The selectivity of diffraction methods makes it possible to trace the reorientation of grains in different phases and structural changes both during plastic deformation [1–3] and during subsequent annealing. In the works of various authors [1,4,5], an additional phase in the form of strong, non-deformable particles leading to scattering of the crystallographic texture has been found. In the case of rolling of immiscible materials, the grains of each metal acquire an orientation corresponding to the symmetry of their structure [6–8]. Texture formation in the hexagonal phase of zirconium and titanium alloys, as well as in cubic metals, is considered in detail in [1–3,9]. However, joint deformation of materials characterized by different crystal structures can lead to different trajectories of grain reorientation and the formation of different types of crystallographic texture depending on the ratio of volume fractions of different phases [1] and the possibility of phase transformations during plastic deformation. Also, the amount and texture of additional phases affect the anisotropy of the properties of the alloy as a whole [1,9,10]. The use of synchrotron radiation and a two-coordinate detector makes it possible not only to study the crystallographic texture of the  $\alpha$ -Zr phase, but also to analyze the predominant orientation of additional phases

present in the alloy in small amounts (up to 2 wt %) [11]. According to [12–17], the main phases in zirconium alloys produced by a Russian company are  $\alpha$ -Zr (a solid solution of niobium in hcp-Zr), which is up to 98 wt.%,  $\beta$ -Zr (a solid solution of about 20 wt.% niobium in bcc-Zr),  $\beta$ -Nb (a solid solution of 10 wt.% Zr in bcc-Nb), and the Laves phase  $Zr(Nb,Fe)_2$  (a hcp phase with periods  $a = 533$  pm and  $c = 874$  pm, structural type C14, space group  $P6_3/mmc$ ) [18–20]. The so-called T-phase  $(Zr,Nb)_2Fe$  with the fcc structure parameter  $a = 1215$  pm [20,21], which has a negative effect on the operational properties of the zirconium alloy, was eliminated by optimizing the alloy composition by reducing the iron content to less than 0.4 wt.% [13,14,17]. The reproducibility of texture data for the  $\alpha$ -Zr phase both for surface layers and for ones thicker than 120  $\mu m$  was illustrated in [22].

The purpose of this work is to analyze the regularities of changes in the structural-phase state and crystallographic texture of multiphase zirconium alloys produced by a Russian company during plastic deformation and heat treatment in the temperature range of 480–640  $^{\circ}C$ .

## 2. Materials and Methods

Samples for research were cut out from cladding tubes and guide channels made of zirconium alloys of these two compositions: Zr-1.0Nb-0.06Fe-0.08O, wt.% (alloy 1) and Zr-1Nb-1.2Sn-0, 35Fe-0.08O, wt.% (alloy 2), respectively. The phase composition and crystallographic texture of various phases present in the alloys was studied, and the regularities of recrystallization of cladding tubes (CTs) and guide channels (GCs) from zirconium alloys was considered as the annealing temperature varied in the range from 480° to 640 °C. Annealing was carried out for 3 h.

X-ray phase analysis was carried out both on X-ray diffractometers and on a synchrotron. To carry out phase analysis, a D8 Discover diffractometer with copper radiation, polycapillary optics, Bragg–Brentano focusing, and a LYNXEYE position-sensitive detector, manufactured by Bruker (Karlsruhe, Germany), was used. To decipher the diffraction pattern, the ICDD PDF2 v2022 database and the Rietveld method were used. A LaB<sub>6</sub> sample was used as a reference. For traditional X-ray texture analysis on a DRON-3 diffractometer with chrome radiation, a composite sample was prepared from narrow tube segments, the middle part of which was perpendicular to the radial (R) direction of the tube, as shown in [22–24]. Further, the investigated sections of tubes will be denoted according to orientation with the surface under study, for example, R-section is a section perpendicular to the R-direction of the tube. The main directions in the tube are radial R, tangential T, and longitudinal L. The calculation of the grain orientation distribution function (ODF) from incomplete direct pole figures (DPFs) (0001), {1010}, {1012}, {1120}, recorded by the sample tilt method, was carried out using LABOTEX software [25,26].

To perform a structural analysis using synchrotron radiation, rings of about 250  $\mu m$  height were cut off from a zirconium tube, both surfaces were ground perpendicular to the axial or longitudinal direction of the tube in order to eliminate layers hardened during electroerosive (EDM) cutting and then etched in a dilute mixture of nitric and hydrofluoric acids to remove the results of mechanical polishing. Samples for “transmission” shooting after grinding and etching were rings 120  $\mu m$  high. The surfaces prepared in this way correspond to the L-sections of the tube [11,22]. The diffraction Debye rings were measured at the synchrotron of the NRC Kurchatov Institute using an experimental XSA (X-ray structure analysis) station (K2.6) equipped with a 2D detector (Rayonix, USA). Transmission photography of foil with a thickness of 120  $\mu m$  was used. The emission wavelength was 0.74 Å. A LaB<sub>6</sub> sample was used as a reference. The Debay rings’ pattern accumulation was carried out for 120–240 s. The diffraction pattern obtained with synchrotron radiation was recalculated to the wavelength of the copper X-ray anode for the convenience of comparing the spectra obtained with different devices. The calculation and construction of the ODF for Debye rings was carried out using the freely distributed MAUD software [27–31]. The ODFs calculated in the MAUD software were uploaded to the MTEX software [32], which makes it possible to construct complete DPFs and rotate them with respect to external directions.

For scanning electron microscopy, plates were cut from the tubes parallel to the tube axis. The investigated surface was perpendicular to the radial direction R-section of the tube [22]. The structure of the material was studied using a Zeiss EVO 50 XVP scanning electron microscope (Carl Zeiss, Oberkochen, Germany). The obtained electron backscatter diffraction (EBSD) data were processed using the EBSD pattern analysis system as part of the Oxford Instruments Nordlys S EBSD pattern detector and the HKL CHANNEL5 software package (Oxford Instruments, UK) [33,34]. EBSD scanning was performed using a step of 0.1–0.2  $\mu\text{m}$  (probe size 0.2 nm) with an average scanning area of  $100 \times 80 \mu\text{m}^2$ .

A comparison of the texture analysis data of the  $\alpha$ -Zr phase of deformed and annealed zirconium alloys was performed using the following methods: electron microscopy, traditional X-ray “in reflection”, and synchrotron “in transmission” carried out following the methodology reported in [22].

### 3. Results

#### 3.1. Phase Analysis

Figures 1 and 2 show the change in the characteristic fragments of the patterns of deformed alloys 1 and 2 as a result of an increase in the annealing temperature from 480 to 640  $^\circ\text{C}$ . The patterns were plotted by summing the intensity over the Debye rings. The intensity scales in Figures 1 and 2 are presented on a logarithmic scale. For the convenience of comparing the patterns, they are shifted along the intensity axis relative to each other. Since we are only interested in weak peaks of additional phases and there is no need to consider intense peaks of the main alpha phase of zirconium, the tops of these peaks are cut off. The full-scale patterns can be viewed in the Supplementary Materials of this article (Figures S1 and S2).

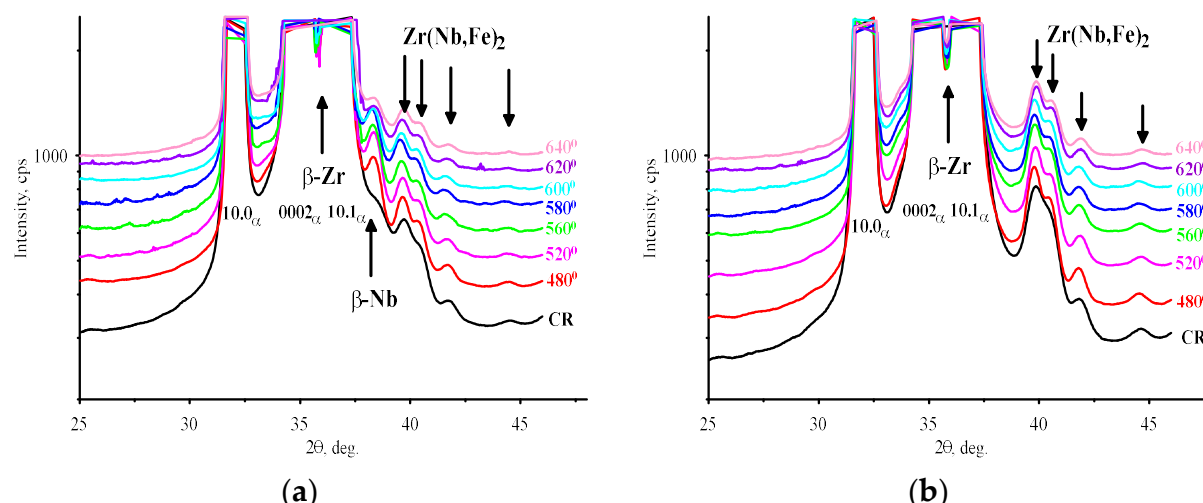


**Figure 1.** Change in the fragment of the diffraction pattern in the range of angles 25–46° of cold-rolled tubes (CR) resulting from an increase in the annealing temperature of alloys 1 (a) and 2 (b). The temperature is indicated near the corresponding pattern.

The choice of the presented fragments is due to the maximum intensity of the peaks of additional phases present in these alloys. In different parts of the patterns of both alloys, the peaks of the  $\beta$ -phases and the Zr(Nb,Fe)<sub>2</sub> intermetallic phase (Laves phase) are seen more or less distinctly. Note that by summing the intensity along the reflection cone (Debye rings), it is possible to eliminate the negative effect of texture on the quantitative phase analysis of the studied samples using the Rietveld method [35]. According to the results obtained, the amount of  $\beta$ -phases in alloy 1 does not exceed 0.4 wt.%, and the intermetallic phase—1.2 wt.%, while in alloy 2 the amount of the Laves phase Zr(Nb,Fe)<sub>2</sub> reaches 1.7 wt.%.

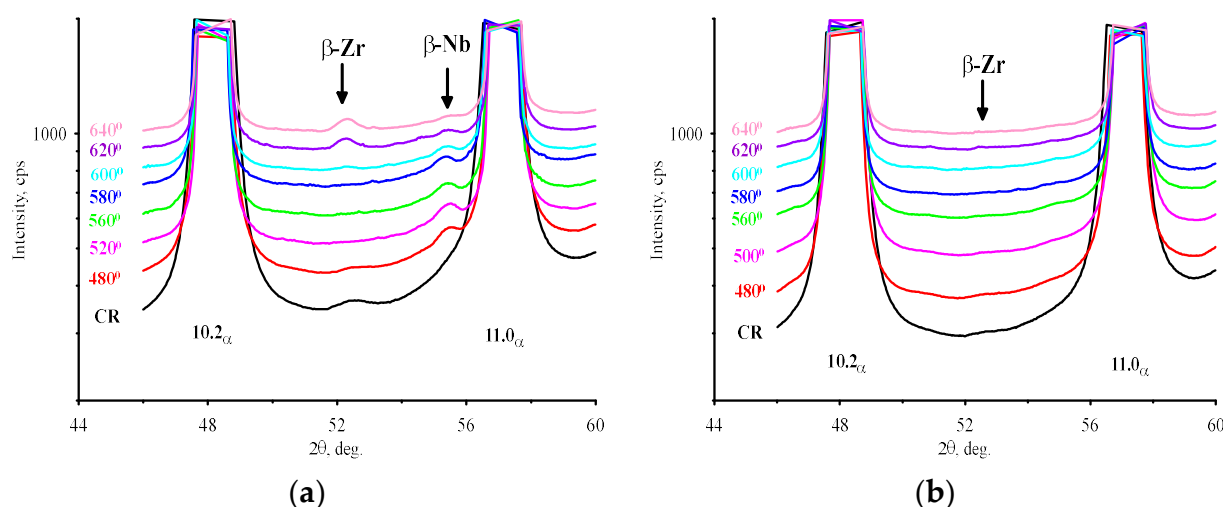


**Figure 2.** Change in the fragment ( $46\text{--}60^\circ$ ) of the diffraction pattern of CR-tubes resulting from an increase in the annealing temperature of alloys 1 (a) and 2 (b).

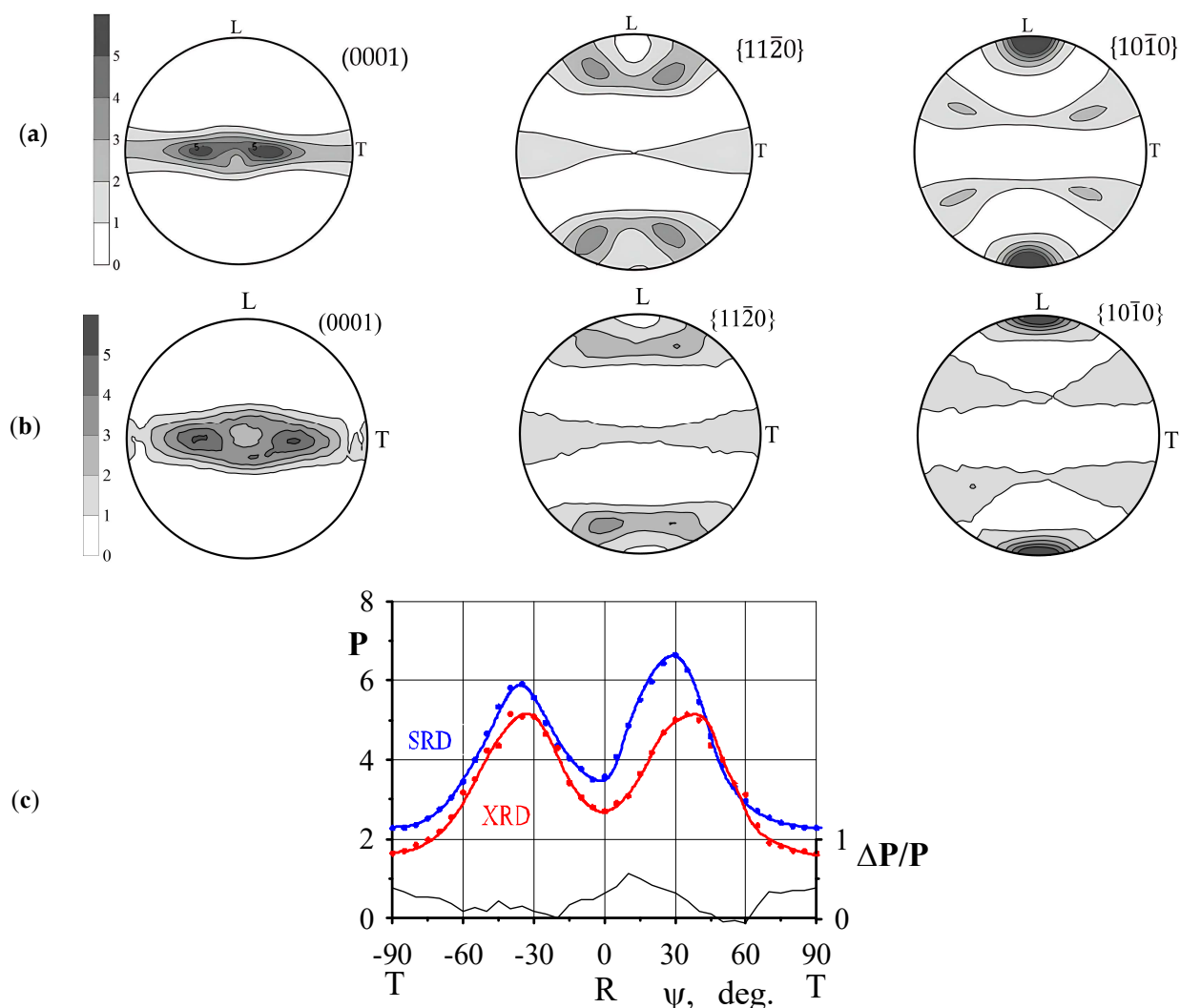
### 3.2. Texture Analysis

#### 3.2.1. Structure and Texture of the $\alpha$ -Phase

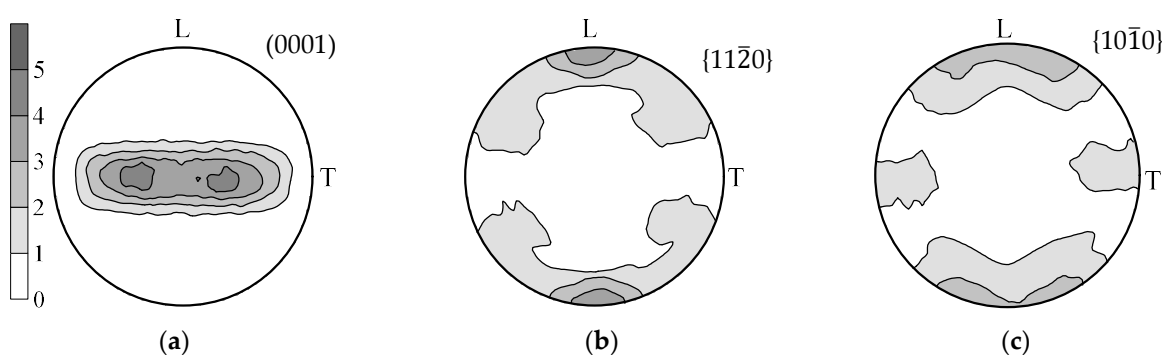
Figure 3 shows typical complete DPFs (0001),  $\{11\bar{2}0\}$ , and  $\{10\bar{1}0\}$  of  $\alpha\text{-Zr}$  phase for a rolled tube from alloy 1, plotted from the results of X-ray surveys on a diffractometer (XRD) and from Debye rings when surveyed with synchrotron radiation (SRD). EBSD maps could not be built for the deformed tube from alloy 1, and hence for the DPFs. According to the DPFs shown in Figure 3, the main texture component of rolled  $\alpha\text{-Zr}$  is  $(0001) \pm 30\text{--}45^\circ R-T <10\bar{1}0>$ , which is clearly fixed by the appearance of a texture maximum against the background of the  $<10\bar{1}0>$  axial component (see Figure 3c). The given distributions of basal axes in the R-T section of a deformed tube indicate a fairly high accuracy of the construction carried out using various software packages. It should also be taken into account that the calculated DPFs characterize different volumes of the material; synchrotron radiation makes it possible to conduct “through-transmission” studies of zirconium foils 120  $\mu\text{m}$  thick, while traditional XRD provides texture information only for thin surface layers up to 20  $\mu\text{m}$  thick.

Figure 4 shows the complete DPFs (0001),  $\{11\bar{2}0\}$  and  $\{10\bar{1}0\}$  of  $\alpha\text{-Zr}$  of recrystallized alloy 1 plotted from X-ray analysis data. The main features presented in Figures 3 and 4 of the DPF (0001) is the broadening of the R-T distribution of the basal axes in the meridional direction and the rotation of the prismatic axes around the basal ones.

The rotation of prismatic axes can be conveniently estimated from the ratio of the pole densities of prismatic axes of different types  $r = P_{11.0}/P_{10.0}$  depending on the annealing temperature (Figure 5). Rotation of prismatic axes, i.e., the implementation of the mechanism of recrystallization through the growth of grains misoriented relative to the deformed matrix by  $30^\circ$  accelerates with increasing temperature. In this case, the occurrence of a phase transformation (PT) at a temperature above the monotectoid transformation additionally facilitates the movement of high-angle boundaries and promotes the growth of grains misoriented with respect to the deformed matrix. Such a mechanism is hindered in the case of an insufficient degree of deformation at the rolling stage (30–50%) [36] in alloy 2. Therefore, in alloy 2, the improvement of the deformed structure mainly occurs through the migration of dislocations to the grain boundaries, i.e., polygonal mechanism, and the subsequent growth of grains corresponding to the orientation of the rolled grains (Figure 5), which practically does not affect the  $r$ .



**Figure 3.** DPFs (0001),  $\{11\bar{2}0\}$  and  $\{10\bar{1}0\}$  of  $\alpha$ -Zr in a deformed tube from alloy 1 for the R-section plotted from synchrotron data (a) and on a diffractometer, (b) as well as the corresponding R-T sections of the DPF (0001). (c) Distributions of basal axes in the R-T section constructed from SRD (blue line) and XRD (red line) measurements of a deformed tube from alloy 1. The thin black line corresponds to the deviation of the pole densities calculated from the data of different DPF measurement methods using this formula:  $\frac{\Delta P}{P} = \frac{P_{SRD} - P_{XRD}}{P_{XRD}}$ .



**Figure 4.** DPFs (0001) (a),  $\{11\bar{2}0\}$  (b) and  $\{10\bar{1}0\}$  (c) of  $\alpha$ -Zr in a recrystallized tube from alloy 1 for the R-section, obtained using the traditional XRD method.

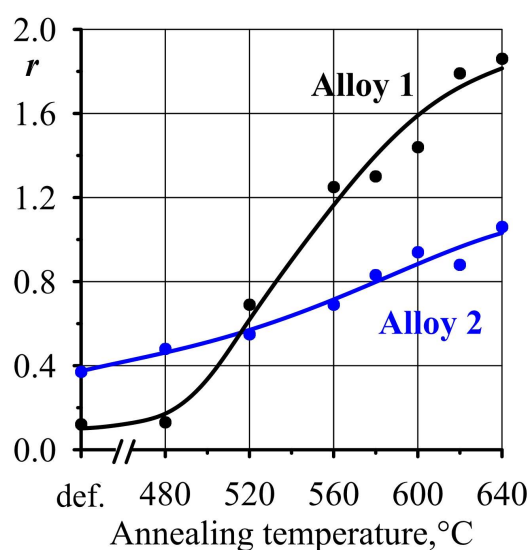
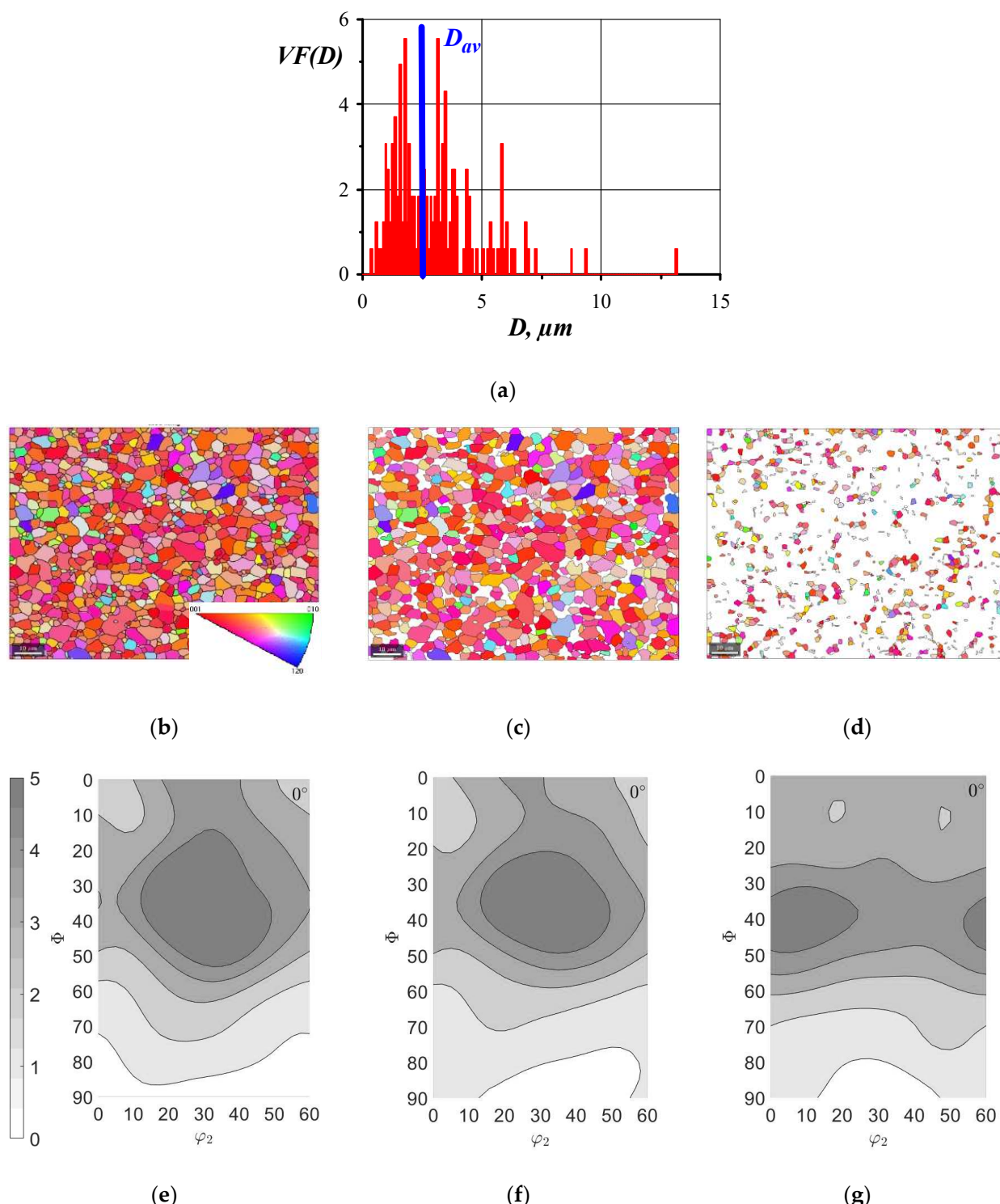


**Figure 5.** Change in the  $r$  ratio with an increase in the annealing temperature for alloys 1 and 2.

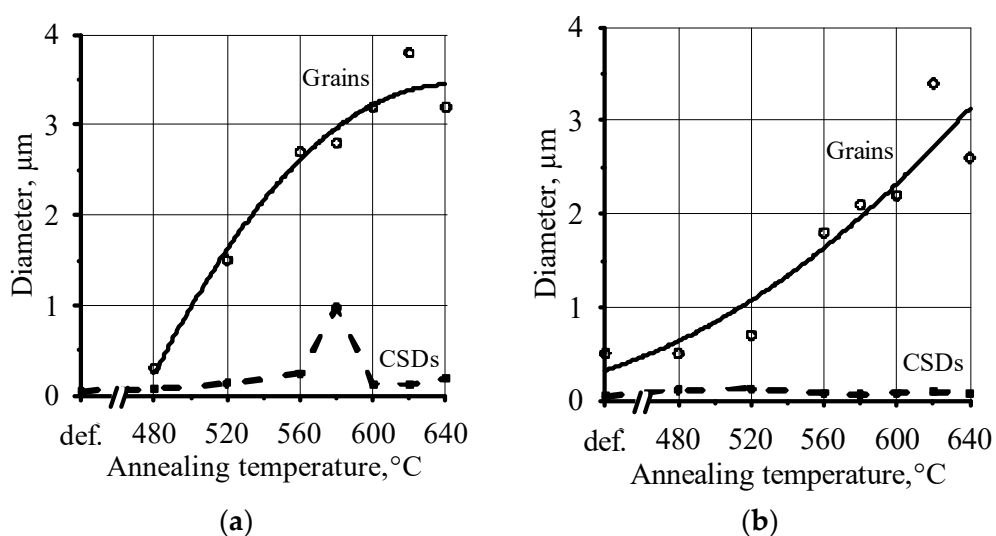
Similar trends in the evolution of the crystallographic texture of zirconium alloys are considered in [36,37]. If, in the first article, the presence of rotation of prismatic axes is assumed, then in the last one, on the contrary, the stability of the deformation texture in the process of primary recrystallization is considered. However, the authors carry out rapid heating of the samples that does not allow the turning mechanism to be activated, as was shown in [38,39].

EBSD maps for all studied samples are presented in the Supplementary Materials in Figures S3 and S4. All results are presented for R-section of the tube. Figure 6a shows a typical grain size distribution based on the EBSD results and provides an estimate of the average grain size  $D_{av}$ , where  $VF$  is the volume fraction of grains with a given size determined for the surface layers 0.1  $\mu\text{m}$  thick. The data are given for alloy 1 annealed at 580 °C. It can be seen from Figure 6a that the grain size varies over a wide range. Let us consider in more detail the distribution of grains over orientations for this sample. Figure 6b shows the complete EBSD map, while Figure 6c,d are maps for large (grain size greater than  $D_{av}$ ) and small grains (grain size less than  $D_{av}$ ), respectively. Below, in Figure 6e–g, the corresponding ODF sections are shown for all grains of the sample (e), and for grains of different sizes, (f)—large and (g)—small. Since the volume fraction of large grains predominates in this sample, the ODF cross section for the entire sample also coincides with the cross section for large grains.

Figure 7 shows the increase in the average grain size calculated from the EBSD data (solid line), as well as the change in the size of coherent scattering domains (CSDs), indicated in the figure by the dotted line. Figure 7b shows a significant increase in the size of the CSDs in alloy 1 at a temperature of 580 °C. Note that the grain size measurement error reaches 1.5  $\mu\text{m}$ , but the CSD size error is 0.001  $\mu\text{m}$ . When the annealing temperature is reached at the beginning of the PT, the size of CSDs decreases again, which is apparently associated with the possibility of separating an additional  $\beta$  phase inside the growing  $\alpha$  grains. In the case of alloy 2, the CSDs can be considered constant within the measurement error, while the grain size continues to grow over the entire annealing temperature range of 480–640 °C, apparently due to the uniform distribution of the finely dispersed particles of Laves phase over the volume.



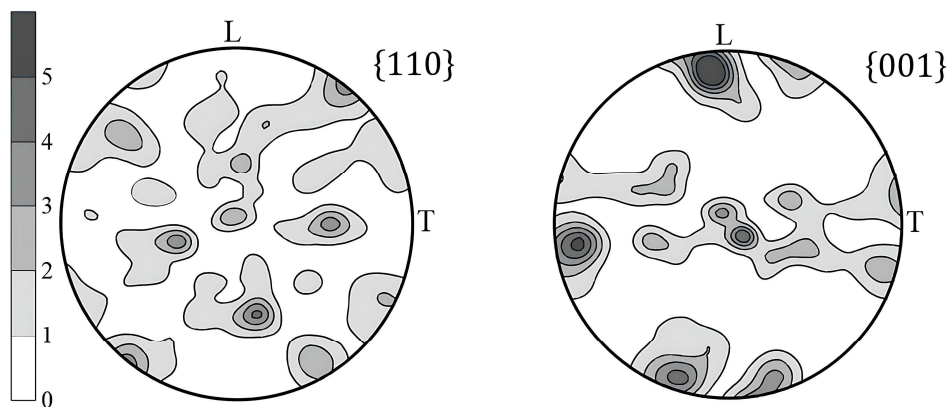
**Figure 6.** Dependence of the grain orientation on their size in the R-section of a tube from alloy 1 annealed at 580 °C for 3 h. (a) Grain size distribution  $D$ , where the blue line corresponds to the average grain size; (b–d) – EBSD-maps for grains: all sizes (b); with sizes greater than  $D_{av}$  (c); with sizes less than  $D_{av}$  (d); (e–g) ODF sections corresponding to cases (b–d).



**Figure 7.** Dependence of grain size and CSD change on the annealing temperature of alloys 1 (a) and 2 (b).

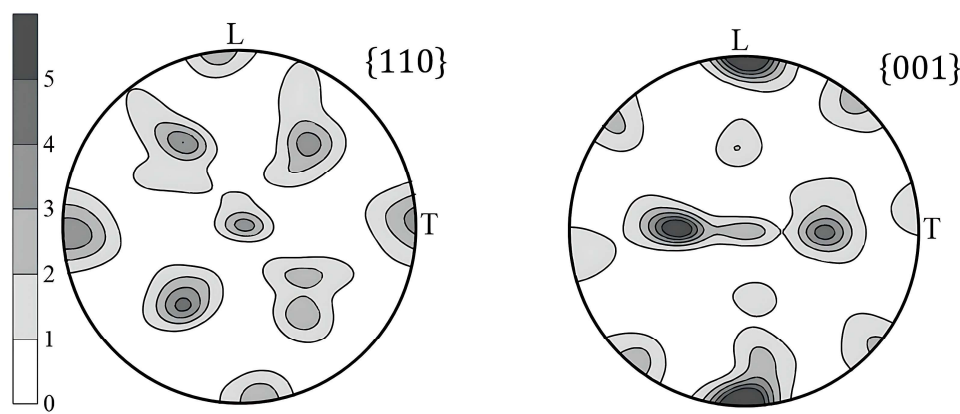
### 3.2.2. Texture of $\beta$ -Phase

Figure 8 shows the complete DPFs {110} and {001} of  $\beta$ -Zr calculated from the Debye rings. If we consider the orientation relationship between  $\alpha$ - and  $\beta$ -phases, for which  $(0001)_\alpha \parallel \{110\}_\beta$ , then it turns out that the  $\{110\}_\beta$  planes correspond to the slopes of texture maxima  $(0001)_\alpha$ , which is confirmed by Figure 8. It is necessary also take into account that the structure and texture of the  $\beta$ -phase is formed during rolling, when the grains of the  $\alpha$ -matrix are also reoriented. Then, the result obtained indicates the development of a dynamic PTs  $\beta \rightarrow \alpha \rightarrow \beta$ , according to which the orientation of the formed grains of the  $\beta$ -Zr phase corresponds to the PT of hcp-Zr into the bcc.



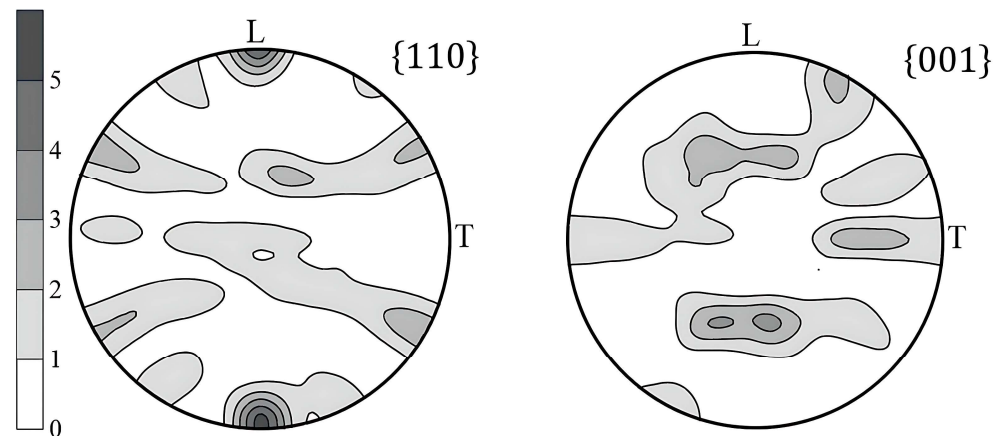
**Figure 8.** Complete DPFs {110} and {001} of  $\beta$ -Zr phase for the R-section of deformed alloy 1.

Figure 9 shows the DPFs {110} and {001} of  $\beta$ -Zr phase, which at a temperature of 480 °C acquire a distinct texture consisting of these three texture components: strong  $\{110\}<001>$  and  $\{110\}<110>$ , and weak  $\{001\}<110>$ .



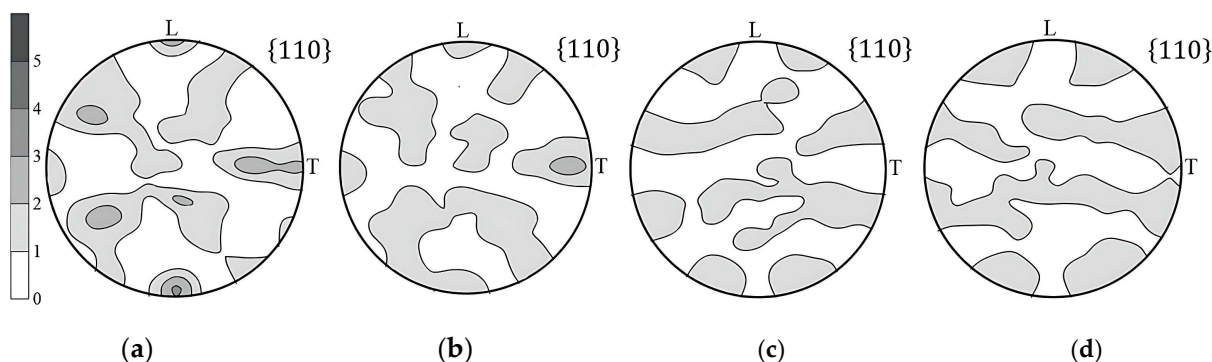
**Figure 9.** Texture of  $\beta$ -Zr for the R-section of alloy 1 annealed at 480  $^{\circ}$ C.

Figure 10 shows the texture of the  $\beta$ -Nb phase, predominantly formed in the deformed grains of the  $\alpha$ -matrix as a result of annealing at a temperature of 480  $^{\circ}$ C, which is formed in strict accordance with the Burgers orientation relation between the hcp and bcc phases. This indicates the independence of the formation of the  $\beta$ -Nb phase in the  $\alpha$ -matrix, i.e., the absence of inheritance of the orientation of the  $\beta$ -Zr phase.



**Figure 10.** Texture of  $\beta$ -Nb for the R-section of alloy 1 annealed at 480  $^{\circ}$ C.

Figure 11 shows the DPFs {110} for  $\beta$ -Zr (Figure 11a,b) and  $\beta$ -Nb (Figure 11c,d). It follows from the presented data that the texture of  $\beta$ -Zr corresponds to the PT in  $\alpha$ -phase grains characterized by the deformation texture (Figure 11a,b), and the texture of  $\beta$ -Nb corresponds to the PT in recrystallized grains. Consequently, when the annealing temperature exceeds the monotectoid transformation temperature in the deformed tube, first of all, the  $\beta$ -Zr phase precipitates in the deformed grains, which are characterized by the rolling texture, and the  $\beta$ -Nb phase, which is characterized by an increased content of niobium, is formed already in the recrystallized grains.



**Figure 11.** DPFs  $\{110\}$  of  $\beta$ -Zr (a,b) and  $\beta$ -Nb (c,d) for R-section of tubes from alloy 1 annealed at  $600\text{ }^{\circ}\text{C}$  (a, c) and  $620\text{ }^{\circ}\text{C}$  (b,d).

### 3.2.3. Laves Phase Texture

Figure 12 shows the DPFs  $(0001)_{\alpha\text{-Zr}}$ ,  $\{11.0\}_{\alpha\text{-Zr}}$ ,  $\{10.0\}_{\alpha\text{-Zr}}$ ,  $(0001)_{LP}$ , where LP is the Laves phase. The circles on the DPF of different phases mark the texture maxima that coincide on the DPFs  $\{11.0\}_{\alpha\text{-Zr}}$  and  $(0001)_{LP}$ .

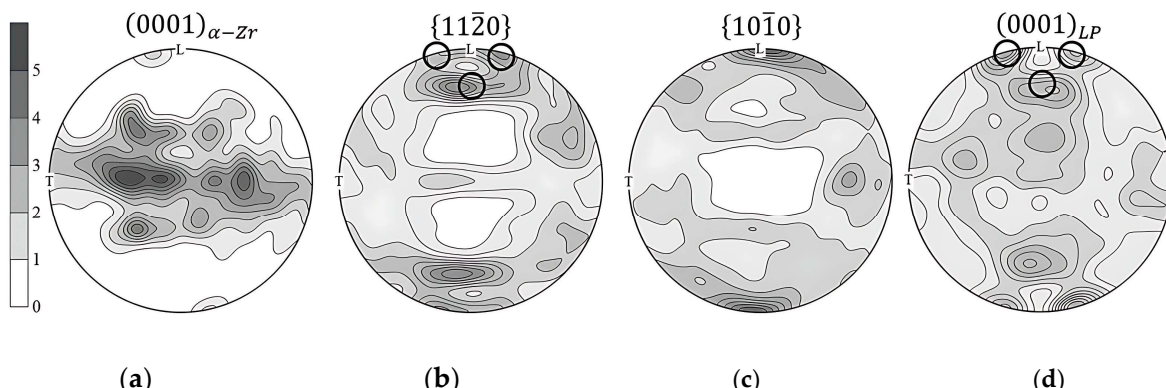


**Figure 12.** Typical DPFs  $(0001)_{\alpha\text{-Zr}}$  (a),  $\{11.0\}_{\alpha\text{-Zr}}$  (b),  $\{10.0\}_{\alpha\text{-Zr}}$  (c),  $(0001)_{LP}$  (d) for alloy 2 annealed at  $560\text{ }^{\circ}\text{C}$ .

According to the results obtained, it is obvious that for the Laves phase and  $\alpha$ -zirconium, the following orientation relation must hold:  $(0001)_{LP} \parallel \{11.0\}_{\alpha\text{-Zr}}$ . However, taking into account the irregularity of the contours of equal pole density on the DPFs of the  $\alpha$ -phase and the decrease in the statistical significance of the data obtained under conditions of significant grain growth, the orientation relation must be verified by electron microscopy.

## 4. Discussion

### 4.1. Changes in the Phase Composition during Deformation and Annealing of Tubes

Using diffraction patterns obtained with synchrotron radiation, a qualitative and quantitative phase analysis of deformed and annealed tubes from alloys 1 and 2 was carried out. The phases detected in the diffraction patterns confirmed the previously known phase composition for alloy 1,  $\alpha$ -Zr,  $\beta$ -Nb,  $\beta$ -Zr and Laves phase (intermetallic compound  $\text{Zr}(\text{Nb},\text{Fe})_2$ ), and for alloy 2,  $\alpha$ -Zr and Laves phase (intermetallic compound  $\text{Zr}(\text{Nb},\text{Fe})_2$ ). In accordance with the Rietveld method and the PDF2 v2022 database, it has been established that the additional phases in Russian zirconium alloys do not exceed 1.6 wt.% in total. Moreover, in deformed alloy 1 there is a  $\beta$ -Zr phase, which, as a result of annealing, turns into a  $\beta$ -Nb phase in accordance with the equilibrium phase diagram of the Zr-Nb alloy. The maximum amount of 0.4 wt.%  $\beta$ -Nb was recorded at a temperature of  $600\text{ }^{\circ}\text{C}$ . However, when annealing above the monotectoid line, the PT of the  $\beta$ -Nb

phase into  $\beta$ -Zr is observed, the content of which increases to 0.6 wt.%. The amount of intermetallic Laves phase in alloy 1 varies from 0.6 to 1.2 wt.%.

Before the final rolling and at its intermediate stages, zirconium tubes are subjected to recrystallization annealing, as a result of which the  $\beta$ -Zr phase (a solid solution of about 20 wt.% niobium in bcc-Zr), which is present in deformed alloy 1 (see Figure 2a), turns into the  $\beta$ -Nb phase, i.e., bcc phase with a high content of niobium in accordance with the equilibrium phase diagram (about 90 wt.% Nb). Then, during plastic deformation, the  $\beta$ -Nb phase transforms into the  $\beta$ -Zr phase, which is observed in the investigated deformed alloy 1 (Figure 2a). As a result of annealing at a temperature of 480 °C for 3 h, the diffusion decomposition of the metastable  $\beta$ -Zr phase into  $\alpha$ -Zr and  $\beta$ -Nb begins, which is expressed in the intensity redistribution between reflections (200) <sub>$\beta$ -Zr</sub> and (200) <sub>$\beta$ -Nb</sub> (see Figure 2a). Along with bcc solid solutions of Nb in bcc-Zr ( $\beta$ -Zr) and Zr in bcc-Nb ( $\beta$ -Nb), alloy 1 contains a small amount (0.1–0.4 wt.%) of the intermetallic phase  $Zr(Nb,Fe)_2$ , reflections from which are retained over the entire investigated annealing temperature range of 480–640 °C.

Both in the deformed and annealed states of alloy 2, the intermetallic phase  $Zr(Nb,Fe)_2$  dominates as an additional phase. In alloy 2, the content of the Laves phase varies from 0.6 to 1.6 wt.%, and the  $\beta$ -phase is absent. In the spectrum of deformed alloy 2 (see Figure 2b), one can see a very weak peak of the  $\beta$ -Zr, which is apparently due to the insufficient amount of iron in the alloy, which participates in the formation of the Laves phase or the increased solubility of iron atoms in the deformed matrix. The formation mechanism of the  $\beta$ -Zr can be the same as in alloy 1, which will be discussed below.

#### 4.2. Changes in the Crystallographic Texture of Different Phases during Deformation and Annealing

In [22], a comparison was made of the DPFs obtained using X-ray radiation of different powers and the EBSD method. It has been established that X-ray methods are more statistically significant, since they allow for obtaining information about grains in larger volumes of the material under study than synchrotron and EBSD methods. Synchrotron methods, like EBSD, are methods that violate statistics (the area under study is 1 or 5 orders of magnitude smaller than the volume reflecting in X-ray diffraction), so the DPFs obtained using them are similar. The performed texture analysis makes it possible to explain the development of the structure of the  $\alpha$ - and  $\beta$ -phases in deformed tubes, as well as in tubes annealed at different temperatures.

##### 4.2.1. Texture $\alpha$ -Zr

The texture of  $\alpha$ -Zr rolled tubes from alloys 1 and 2 is characterized by the texture components  $(0001) \pm 30\text{--}45^\circ R-T <10\bar{1}0>$ . During annealing, the distribution of both basal axes and prismatic ones can change [36]. At an annealing temperature of 480 °C, the structure is improved by the migration of point defects and dislocations to the grain boundaries, as a result of which the predominant grain orientation is retained. At the stage of recrystallization, at a temperature above 560 °C, the growth of grains begins, the orientation of the basal axes of which corresponds to the slopes of texture maxima on DPF (0001) [36–38] because of their increased work hardening. As a result, the DPF (0001) broadens in the meridional direction. When using synchrotron data (for example, Figure 12) on the DPF (0001) <sub>$\alpha$ -Zr</sub> for alloy 2, it annealed at a temperature of 560 °C and the formation of additional texture maxima was observed, which formed on their slopes facing the L-direction. The fragmentation of the DPF (0001) indicates a decrease in the statistical significance of the results obtained.

During recrystallization (Figures 4–6), the rotation of prismatic axes is activated, i.e., the mechanism of recrystallization is realized by the growth of grains misoriented relative to the deformed matrix by 30°. This rotation is enhanced with an increase in the annealing temperature up to the temperature of the monotectoid transformation  $T_m$  (see Figure 5). The activation of the PT at a temperature above  $T_m$  additionally facilitates the

movement of high-angle boundaries and also promotes the growth of grains misoriented with respect to the deformed matrix. Such a mechanism is hindered in alloy 2 in the case of an insufficient degree of deformation at the rolling stage (less than 30–50%) [37,38]. Therefore, in alloy 2, the improvement of the deformed structure mainly occurs through the migration of dislocations to the grain boundaries, i.e., polygonal mechanism, and the subsequent growth of grains corresponding to the orientation of the rolled grains (Figure 5), which confirms the smaller slope of the dependence of  $r$  on the annealing temperature. For both alloys, the recrystallization texture is described by the components  $(0001) \pm 30\text{--}40^\circ R-T<11\bar{2}0>$ .

The analysis of EBSD maps showed (Figure 6) that grains characterized by a large size have a recrystallization texture, while fine grains have a deformation texture. In small grains, the process of polygonization has passed, but the movement of their boundaries is hindered by grains that are misoriented relative to the deformed matrix by  $30^\circ$  around the basal axes, since the rate of movement of boundaries with a misorientation angle of  $30^\circ$  is the maximum in a hexagonal structure [38]. Thus, it is strictly shown that the structure of recrystallized alloy 1 consists of grains of different sizes, and it is difficult for large grains to grow further because of small grains with a polygonal structure, since for their absorption the surface of a large grain must be curved so that its energy will increase significantly. Therefore, such a structure should be very stable at the stage of primary recrystallization. A change in the grain size will become possible only if the temperature exceeds the monotectoid transformation line in the equilibrium phase diagram.

The synchrotron data made it possible to establish that the CSDs for both alloys was at the level of one micrometer, and only for alloy 1, annealed precisely at a temperature of  $580^\circ\text{C}$ , does it sharply increase, corresponding to the most intensive growth of recrystallized grains. In this case, in both alloys, apparently, the presence of an additional Laves phase prevents changes in the sizes of CSDs and grains.

Similar trends in the evolution of the crystallographic texture of  $\alpha\text{-Zr}$  are considered in [39–41]. If in the first two articles the presence of rotation of prismatic axes is assumed, then in the last article, on the contrary, the stability of the deformation texture in the process of primary recrystallization is considered. However, the authors of [41] carry out rapid heating of the samples, which does not allow the turning mechanism to be activated, as was shown in [36,37]. The presence of grains of different orientations and sizes in the recrystallized material must be taken into account when predicting the behavior of the material during operation.

#### 4.2.2. Texture of $\beta\text{-Zr}$ and $\beta\text{-Nb}$

Let us consider the process of changing the structure and texture of  $\beta$ -phase for alloy 1 during plastic deformation and heat treatment. The  $\beta\text{-Zr}$  phase was registered in the deformed tube from alloy 1 (Figure 2). In the case of independent deformation of the phases, each of them can acquire its own orientation in accordance with the laws of crystallography and active mechanisms of plastic deformation. The rolling texture of bcc metals is the  $\{001\}<110>$  component. However, it is absent in the texture of the deformed sample (see Figure 8), which indicates a different mechanism for the formation of the  $\beta\text{-Zr}$  texture. If the  $\beta$ -phase was deformed independently of the surrounding  $\alpha$ -phase, then the texture component  $\{001\}<110>$  should prevail in the rolling texture. If we assume that fine grains of the  $\beta$ -phase are riveted during rolling owing to the accumulation of defects, then they become thermodynamically unstable, leading to the occurrence of the  $\beta \rightarrow \alpha$  PT in them. An increased concentration of niobium in the  $\beta$ -phase and stress relaxation as a result of the PT provide the inverse  $\alpha \rightarrow \beta$  PT. The dynamic PTs also makes it possible to explain the fact that, as a result of plastic deformation, the  $\beta\text{-Nb}$  phase with 90% Nb transforms into the  $\beta\text{-Zr}$  phase containing about 20% Nb. Of course, redistribution of elements is possible in deformed structures, but the change from 90 to 20 wt.% is too large for diffusion processes. Therefore, the mechanism of dynamic  $\beta \rightarrow \alpha \rightarrow \beta$  PTs seems to be the most realistic, as a result of which the hardened phases are unstable and undergo a

transformation, and after relaxation and a change in the concentration of elements in the solid solution, they undergo a reverse PT. Such a process provides an accelerated change in the concentration of niobium in the  $\beta$ -phase from 90 to 20%. Then the  $\beta$ -zirconium phase should be characterized by the crystallographic texture of the PTs, which are realized while observing the orientational Burgers relation:  $(0001) \parallel \{110\}$  and  $\langle 11\bar{2}0 \rangle \parallel \langle 111 \rangle$ , as shown in Figure 8.

The  $\{110\}\langle 001 \rangle$  orientation of the  $\beta$ -zirconium phase in alloy 1 annealed at 480 °C (see Figure 9) is the most intense. Generally [39], grains of the bcc phase with the  $\{110\}\langle 001 \rangle$  orientation appear at the stage of primary recrystallization and can become centers of secondary recrystallization in the presence of neighboring grains. This is because grains with the  $\{110\}\langle 001 \rangle$  orientation are formed earlier than others during primary recrystallization in the most distorted regions and become the largest by the end of primary recrystallization. A sharp change in the shape of the DPFs  $\{110\}$  and  $\{001\}$  (compare Figures 8 and 9) indicates the occurrence of the recrystallization phase in fine grains of  $\beta$ -Zr. The latter is possible under conditions when stresses develop in deformed  $\beta$ -grains as a result of heating the sample to 480 °C, owing to differences in the thermal expansion coefficients of  $\alpha$ - and  $\beta$ -phases.

According to the equilibrium diagram of states of Zr-Nb at a temperature of 480 °C, the  $\beta$ -Zr phase is metastable, as a result of which, after annealing for 3 h, the formation of a new stable bcc  $\beta$ -Nb phase is observed in the alloy. The texture of  $\beta$ -Nb is shown in Figure 10. The given DPF  $\{110\}$  indicates the formation of a solid solution of  $\beta$ -Nb in grains with a rolling texture of  $\alpha$ -Zr strictly in accordance with the known orientation relationship between bcc and hcp structures. Thus, it can be concluded that  $\beta$ -Nb grains are predominantly formed not from the recrystallized  $\beta$ -Zr phase, but in different regions of the deformed matrix where fluctuations in the elemental composition of the alloy or inhomogeneity of the defect structure are observed in accordance with the laws of diffusion.

An increase in the annealing temperature above the monotectoid line contributes to an increase in the grain size, a decrease in the statistical significance of the results obtained, but nevertheless, if we compare the DPFs  $\{110\}$  presented in Figure 11, we can see that  $\beta$ -Zr has an orientation corresponding to the deformed  $\alpha$ -phase, and  $\beta$ -Nb – recrystallized  $\alpha$ -phase. Apparently,  $\beta$ -Zr forms earlier, until recrystallization has completely occurred, and the isolation of  $\beta$ -Nb (with large differences in the elemental composition of the  $\alpha$ - and  $\beta$ -phases) requires time for diffusion processes to occur.

## 5. Conclusions

1. Using data obtained with synchrotron radiation, a phase analysis of deformed and annealed zirconium-based alloys was carried out. The main phase of the investigated alloys was a solid solution of alloying elements in the hcp structure of  $\alpha$ -Zr. The Zr-1Nb-1.2Sn-0.35Fe-0.08O alloy, wt.% was characterized by the presence of an additional stable Laves phase ( $(Zr,Nb)Fe_2$ ), which retained its structure in the deformed state and during subsequent annealing in the temperature range of 480–640 °C. In the deformed Zr-1.0Nb-0.06Fe-0.08O alloy, additional phases were solid solutions in the bcc structure with different elemental compositions ( $\beta$ -Nb,  $\beta$ -Zr) and the Laves phase. The content of additional phases did not exceed 1.6 wt.%.
2. An algorithm for studying the crystallographic texture of materials using Debye rings obtained on synchrotron X-rays when photographing foils up to 120  $\mu$ m thick were optimized. Orientation grain distribution functions (ODFs) and complete direct pole figures (DPFs) were constructed for the  $\alpha$ -phase and for phases present in small amounts in the material for deformed and annealed zirconium alloys.
3. It was shown that the rolling texture of  $\alpha$ -Zr for the inner layers of the material corresponded to that measured earlier for the surface layers using X-ray analysis, namely, the following rolling texture was observed in the volume of the rolled material:  $(0001) \pm 30\text{--}45^\circ \text{RD-TD} \langle 10\bar{1}0 \rangle$ . As a result of recrystallization of  $\alpha$ -Zr, the deformation texture was replaced by the recrystallization texture  $(0001) \pm 30\text{--}45^\circ \text{RD-TD} \langle 11\bar{2}0 \rangle$ ,

which was due to the absorption of the deformed matrix by recrystallized grains misoriented, with respect to the initial grains, by a rotation of 30° around the basal axes. Based on the results of the synchrotron study, dependences of the ratio of the pole densities of the  $<11\bar{2}0>$  and  $<10\bar{1}0>$  axes oriented along the tube rolling direction were obtained, characterizing the completeness of the recrystallization at different annealing temperatures. For the Zr-1.0Nb-0.06Fe-0.08O alloy, annealed at a temperature of 580 °C for 3 h, the maximum domain of coherent scattering was found, which is an order of magnitude higher than the domains at other annealing temperatures.

4. It has been established that during plastic deformation of the alloy, a dynamic phase transformation  $\beta\text{-Nb}\rightarrow\alpha\text{-Zr}\rightarrow\beta\text{-Zr}$  is observed, as a result of which the content of niobium in the bcc phase changes from 90 to 20% and the formation of a texture of phase transformations in  $\beta\text{-Zr}$  is observed.
5. It was found that at an annealing temperature of 480 °C for 3 h, the main texture component  $\{110\}<001>$ , characteristic of the recrystallization of bcc metals, was formed in  $\beta\text{-Zr}$ . The observed recrystallization of the finely dispersed  $\beta\text{-Zr}$  phase may be due to its constraint in the  $\alpha$ -matrix.
6. It has been established that the  $\beta\text{-Nb}$  phase acquires a predominant orientation, corresponding to the phase transformation in the  $\alpha$ -matrix, as a result of annealing the Zr-1.0Nb-0.06Fe-0.08O alloy at a temperature of 480 °C—3 h; the texture component  $\{110\}<001>$  corresponding to the recrystallization texture was weak. As the annealing temperature rises above the monotectic temperature, the  $\beta\text{-Zr}$  phase is formed in deformed grains, and the  $\beta\text{-Nb}$  phase is formed in recrystallized grains.
7. It was shown that the amount, structure, and texture of the intermetallic phase are stable both in deformed alloys and when the annealing temperature is increased to 640 °C.

**Supplementary Materials:** The following supporting information can be downloaded at: <https://www.mdpi.com/article/10.3390/met13101784/s1>. Figure S1. Change in the diffraction pattern of the deformed alloy 1 with increasing annealing temperature. Figure S2. Change in the diffraction pattern of the deformed alloy 2 with increasing annealing temperature. Figure S3. Change in the EBSD-map of the deformed alloy 1 with increasing annealing temperature. Figure S4. Change in the EBSD-map of the deformed alloy 2 with increasing annealing temperature.

**Author Contributions:** Conceptualization, M.I.; Methodology, M.I. and O.K.; software, M.I., O.K., K.K.; validation, O.K., A.B. and K.K.; Formal analysis, M.I., O.K., K.K. and A.B.; Investigation, K.K., I.K., R.S., P.D. and V.F.; Resources, V.F., K.K. and R.S.; Data curation, K.K.; Writing—original draft preparation, M.I., O.K. and K.K.; Writing—review and editing, M.I.; Visualization, O.K., K.K., A.B.; Supervision, M.I. All authors have read and agreed to the published version of the manuscript.

**Funding:** This research was funded by the Ministry of Science and Higher Education of the Russian Federation, grant number No. 075-15-2021-1352.

**Data Availability Statement:** The data are available from the authors upon reasonable request.

**Acknowledgments:** The authors express their gratitude for the provision of samples for research to the Joint-Stock Company "High-Tech Research Institute of Inorganic Materials named after Academician A.A. Bochvar".

**Conflicts of Interest:** The authors declare no conflict of interest.

## References

1. Kocks, U.F.; Tome, C.N.; Wenk, H.R. *Texture and Anisotropy*; Cambridge University Press: Cambridge, UK, 1998; 675p.
2. Vishnyakov, Y.D.; Babareko, A.A.; Vladimirov, S.A.; Egiz, I.V. *Theory of Texture Formation in Metals and Alloys*; Nauka: Moscow, Russia, 1979; 344p. (In Russian)
3. Perlovich, Y.; Bunge, H.J.; Isaenkova, M. Structure inhomogeneity of rolled textured niobium. *Z. Metallk. Mater. Res. Adv. Tech.* **2000**, *91*, 149–159.

4. Bolmaro, R.E.; Guerra, F.M.; Kocks, U.F.; Browning, R.V.; Dawson, P.R.; Embury, J.D.; Poole, W. On plastic strain distribution and texture development in fiber composites. *Acta Metall. Mater.* **1993**, *41*, 1893–1905. [[CrossRef](#)]
5. Poole, W.J.; Embury, J.D.; Kocks, U.F.; Bolmaro, R.E.; Embury, J.D. Texture Development in Cu-W Composites. In *Metal Matrix Composites: Processing, Microstructure and Properties*; Hansen, N., Jensen, D., Leffers, T., Lilholt, H., Lorentzen, T., Pedersen, A., Pedersen O., B., Ralph, B., Eds.; Risø National Laboratory: Roskilde, Denmark, 1991; pp. 587–593.
6. Raabe, D.; Heringhaus, F.; Hangen, U.; Gottstein, G. Investigation of a Cu-20 mass% Nb in situ composite. *Z. Metallk.* **1995**, *86*, 405–415.
7. Biselli, C.; Morris, D.G. Microstructure and strength of Cu-Fe in situ composites after very high drawing strains. *Acta Mater.* **1996**, *44*, 493–504. [[CrossRef](#)]
8. Aksyonova, T.D.; Boruta, S.S.; Perlovich, Y.A.; Rusakov, A.A.; Kutepov, V.P.; Sytnikov, V.E.; Shikov A., K.; Vorobushkin, V.A. Formation of the structure of Nb and Nb<sub>3</sub>Sn in composite wires. *Issues Nucl. Sci. Technology. Ser. At. Mater.* **1985**, *21*, 58–62. (In Russian)
9. Lutjering, G.; Williams, J.C. *Titanium*; Springer: Heidelberg, Germany, 2007; 442p.
10. Isaenkova, M.G.; Krymskaya, O.A.; Babich, Y.A.; Medvedev, P.N. Effect of the Crystallographic Texture in the  $\alpha$  Phase on the Anisotropy of the Properties of Pseudo- $\alpha$  and ( $\alpha + \beta$ ) Titanium Alloy Sheets. *Russ. Metall. Met.* **2021**, *2021*, 430–436. [[CrossRef](#)]
11. Isaenkova, M.G.; Petrov, M.I.; Kozlov, I.V.; Bogomolova, A.V. Structural features of hydrogenated E110opt and E635 tubes. *Non-Ferr. Met.* **2023**, *1*, 41–48. [[CrossRef](#)]
12. Zaimovsky, A.S.; Nikulina, A.V.; Reshetnikov, N.G. *Zirconium Alloys in Nuclear Power Engineering*; Energoizdat: Moscow, Russia, 1994; 256p. (In Russian)
13. Shishov, V.N.; Peregud, M.M.; Nikulina, A.V.; Shebalov, P.V. Influence of Zirconium Alloy Chemical Composition on Microstructure Formation and Irradiation Growth. In Proceedings of the 13th International Symposium on Zirconium in the Nuclear Industry, Annecy, France, 10–14 June 2001; pp. 758–779.
14. Shishov, V.N. The Evolution of Microstructure and Deformation Stability in Zr-Nb-(Sn,Fe) Alloys Under Neutron Irradiation. In Proceedings of the Zirconium in the Nuclear Industry: 16th International Symposium, Chengdu, China; 2011; pp. 37–66. [[CrossRef](#)]
15. Alekseeva, Z.M.; Korotkova, N.V. Isothermal phase diagrams of Zr-Nb-Fe in the temperature range 1600–850 °C. *Russ. Metall. Met.* **1989**, *1*, 199–205. (In Russian)
16. Kobylyansky, G.P.; Novoselov, A.E.; Obukhov, A.V.; Ostrovsky, Z.E.; Shishov, V.N.; Nikulina, A.V.; Markelov, V.A. Radiation damage to the Zirconium alloy E635 in structural elements of VVER-1000 fuel assemblies. *Inorg. Mater. Appl. Res.* **2009**, *3*, 30–41. (In Russian)
17. Nikulina, A.V.; Markelov, V.A.; Novikov, V.V.; Peregud, M.M.; Konkov, V.F.; Sablin, M.N.; Mileshkina, O.Y. E110M Zirconium alloy for fuel claddings of VVER-1000 and PWR reactors. *VANT Ser. Mater. Sci. New Mater.* **2018**, *4*, 22–29. (In Russian)
18. Averin, S.; Panchenko, V.; Kozlov, A.; Sinelnikov, L.; Shishov, V.; Nikulina, A. Evolution of Dislocation and Precipitate Structure in Zr Alloys Under Long-Term Irradiation. In Proceedings of the Zirconium in the Nuclear Industry: Twelfth International Symposium ASTM STP, West Conshohocken, PA, USA, January 2000; 2000; Volume 1354, pp. 105–121. [[CrossRef](#)]
19. Averin, S.A.; Panchenko, V.L.; Tsygintsev, V.A.; Pastukhov, V.I. Evolution of the structure of the Zr-2.5%Nb alloy during long-term low-temperature neutron irradiation. *Met. Sci. Heat Treat. Met.* **2021**, *3*, 75–80. (In Russian)
20. Toffolon, C.; Brachet, J.-C.; Servant, C.; Legras, L.; Charquet, D.; Barberis, P.; Mardon, J. Experimental Study and Preliminary Thermodynamic Calculations of the Pseudo-Ternary Zr-Nb-Fe-(O,Sn) System. In *Proceedings of the Zirconium in the Nuclear Industry: Thirteenth International Symposium, ASTM STP*; ASTM International: West Conshohocken, PA, USA, 2002; Volume 1423, pp. 361–383. [[CrossRef](#)]
21. Ramos, C.; Saragovi, C.; Granovsky, M.S. Some new experimental results on the Zr-Nb-Fe system. *J. Nucl. Mater.* **2007**, *366*, 198–205. [[CrossRef](#)]
22. Isaenkova, M.G.; Krymskaya, O.A.; Klyukova, K.E.; Bogomolova, A.V.; Dzhumaev, P.S.; Kozlov, I.V.; Fesenko, V.A. Comparison of the texture analysis results of zirconium alloys according to the data of backscattered electron diffraction and X-ray radiation of different power. *Lett. Mater.* **2023**, *13*(4), 341–346.
23. Isaenkova, M.; Perlovich, Y.; Fesenko, V. Modern methods of experimental construction of texture complete direct pole figures by using X-ray data. *IOP Conf. Ser. Mater. Sci. Eng.* **2016**, *130*, 012055. [[CrossRef](#)]
24. Perlovich, Y.A.; Isaenkova, M.G.; Krymskaya, O.A.; Fesenko, V.A.; Babich, Y.A. Optimization of the procedure for determining integral texture parameters of products from zirconium-based alloys using the orientation distribution function. *IOP Conf. Ser. Mater. Sci. Eng.* **2016**, *130*, 012056. [[CrossRef](#)]
25. Pawlik, K. Determination of the orientation distribution function from pole figures in arbitrarily defined cells. *Phys. Status Solidi B* **1986**, *134*, 477–483. [[CrossRef](#)]
26. LaboTex. Version 3.0; LaboSoft: Krakow, Poland. Available online: <http://www.labosoft.com.pl> (accessed on 10 August 2023).
27. Lutterotti, L.; Vasin, R.; Wenk, H.-R. Rietveld texture analysis from synchrotron diffraction images. I. Calibration and basic analysis. *Powder Diffr.* **2014**, *29*, 76–84. [[CrossRef](#)]
28. Wenk, H.-R.; Lutterotti, L.; Kaercher, P.; Kanitpanyacharoen, W.; Miyagi, L.; Vasin, R. Rietveld texture analysis from synchrotron diffraction images. II. Complex multiphase materials and diamond anvil cell experiments. *Powder Diffr.* **2014**, *29*, 220–232. [[CrossRef](#)]

29. Benatti, E.A.; De Vincentis, N.S.; Al-Hamday, N.; Schell, N.; Brokmeier, H.-G.; Avalos, M.; Bolmaro, R.E. Generalized pole figures from post-processing whole Debye–Scherrer patterns for microstructural analysis on deformed materials. *J. Synchrotron Radiat.* **2022**, *29*, 732–748. [[CrossRef](#)]
30. Von Dreele, R.B. Quantitative texture analysis by Rietveld refinement. *J. Appl. Crystallogr.* **1997**, *30*, 517–525. [[CrossRef](#)]
31. Saville, A.I.; Creuziger, A.; Mitchell, E.B.; Vogel, S.C.; Benzing, J.T.; Klemm-Toole, J.; Clarke, K.D.; Clarke, A.J. MAUD Rietveld Refinement Software for Neutron Diffraction Texture Studies of Single- and Dual-Phase Materials. *Integr. Mater. Manuf. Innov.* **2021**, *10*, 461–487. [[CrossRef](#)]
32. MTEX Software for Analyzing and Modeling Crystallographic Textures by Means of EBSD or Pole Figure Data (TU Chemnitz, Germany). Available online: <https://mTEX-toolbox.github.io/Documentation> (accessed on 10 August 2023).
33. Engler, O.; Randle, V. *Introduction to Texture Analysis*; CRC Press LLC: Boca Raton, FL, USA, 2009; 488p. [[CrossRef](#)]
34. Tsai, S.-P.; Konijnenberg, P.J.; Gonzalez, I.; Hartke, S.; Griffiths, T.A.; Herbig, M.; Kawano-Miyata, K.; Taniyama, A.; Sano, N.; Zaefferer, S. Development of a new, fully automated system for electron backscatter diffraction (EBSD)-based large volume three-dimensional microstructure mapping using serial sectioning by mechanical polishing, and its application to the analysis of special boundaries in 316L stainless steel. *Rev. Sci. Instrum. USA* **2022**, *93*, 093707. [[CrossRef](#)]
35. Rietveld, H.M. The Rietveld Method: A Retrospection. *Z. Krist.* **2010**, *225*, 545–547. [[CrossRef](#)]
36. Isaenkova, M.G.; Klyukova, K.E.; Krymskaya, O.A.; Fesenko, V.A.; Dzhumaev, P.S. Regularities of changes in the structure and texture of sheets and tubes made of E635 and E110 alloys of modified composition according to the results of X-ray and electron microscopic analysis. *VANT Ser. Mater. Sci. New Mater.* **2023**, *1*, 15–33. (In Russian)
37. Klyukova, K.E.; Isaenkova, M.G.; Krymskaya, O.A.; Fesenko, V.A. Crystallographic texture and structure formed in rolled sheets of zirconium alloys during annealing. *Tsvetnye Met.* **2022**, *10*, 19–26. [[CrossRef](#)]
38. Gorelik, S.S. *Recrystallization of Metals and Alloys*; Metallurgy: Moscow, Russia, 1967; 402p. (In Russian)
39. Zhu, K.Y.; Bacroix, B.; Chauveau, T.; Chaubet, D.; Castelnau, O. Texture Evolution and Associated Nucleation and Growth Mechanisms during Annealing of a Zr Alloy. *Metall. Mater. Trans. A* **2009**, *40*, 2423–2434. [[CrossRef](#)]
40. Jung, T.-S.; Jang, H.; Mok, Y.-K.; Yoo, J.-S. Analysis of EBSD image quality related to microstructure evolution in zirconium-niobium cladding to quantify the degree of recrystallization. *J. Nucl. Mater.* **2018**, *509*, 188–197. [[CrossRef](#)]
41. Gerspach, F.; Bozzolo, N.; Wagner, F. About texture stability during primary recrystallization of cold-rolled low alloyed zirconium. *Scr. Mater.* **2009**, *60*, 203–206. [[CrossRef](#)]

**Disclaimer/Publisher’s Note:** The statements, opinions and data contained in all publications are solely those of the individual author(s) and contributor(s) and not of MDPI and/or the editor(s). MDPI and/or the editor(s) disclaim responsibility for any injury to people or property resulting from any ideas, methods, instructions or products referred to in the content.